Acta Materialia 211 (2021) 116886

Contents lists available at ScienceDirect

Acta Materialia

journal homepage: www.elsevier.com/locate/actamat

Full length article

Temperature-dependent mechanisms of dislocation–twin boundary interactions in Ni-based equiatomic alloys

Sho Hayakawa, Haixuan Xu*

Department of Materials Science and Engineering, The University of Tennessee, Knoxville, TN 37996, United States

ARTICLE INFO

Article history:
Received 22 November 2020
Revised 3 April 2021
Accepted 6 April 2021
Available online 12 April 2021

ABSTRACT

The high entropy alloy FeNiCoCrMn and its subsets have exhibited an unusual combination of strength and ductility dependance on temperature, showing a significant increase in ductility as temperature decreases. This phenomenon is intriguing, and the underlying mechanism is critical for understanding the mechanical properties of these materials. Here, we investigate the interaction between a screw dislocation and a coherent twin boundary in Ni-based equiatomic alloys using atomistic simulations. We find that the dominant mechanism for this interaction changes as a function of temperature, which could be one of the underlying causes of the enhanced ductility at cryogenic temperatures in these alloys. Further investigations reveal the interaction's temperature dependence arises from a critical parameter related to the stacking fault energy and the distance between the Shockley partial dislocations. The insights extracted herein contribute to a fundamental understanding of plastic deformation in Ni-based equiatomic alloys and can be utilized for developing design strategies to achieve superior strength and ductility in structural materials.

1. Introduction

High entropy alloys (HEAs) have exhibited some exceptional mechanical properties compared to conventional dilute alloys [1–7]. For instance, the quinary equiatomic FeNiCoCrMn alloy possesses an excellent balance between the strength and ductility even at cryogenic temperatures [2,8,9]; an unusual but desirable phenomenon. Moreover, some subsets of FeNiCoCrMn, such as FeNi and FeNiCoCr [10], have also shown similar behavior. This combination of strength and ductility is very attractive for structural materials because these two properties are mutually exclusive in most conventional alloys [11]. Therefore, it is essential to reveal the underlying mechanism that is responsible for the increase in both strength and ductility in these alloys.

Deformation twinning in FeNiCoCrMn and its subset alloys has been reported in previous experimental studies, particularly at 77 K [2,8,12–15], and is considered a crucial microstructural feature in these alloys. A recent study found that the true plastic strains for the onset of deformation twinning in FeNiCoCrMn are ~25%, ~16%, and ~8% at 293, 198, and 77 K, respectively [16]. This suggests that the early onset of deformation twinning at low temperatures could lead to an increase in the ductility, while dislocation glide plays a more significant role at higher temperatures. However, Laplanche et al. [17] evaluated the volume fraction of twins in FeNiCoCrMn formed during the plastic deformation and estimated the contribution from deformation twins to the overall tensile strain, and found the contribution was less than 3% of the total true strain of the specimen. This indicates that deformation twinning alone is insufficient and other microstructural features, e.g., dislocations, could be involved in the enhanced ductility at cryogenic temperatures in FeNiCoCrMn and its subset alloys. Meanwhile, twin boundaries are strong obstacles for the motion of dislocations. Indeed, experimental studies have reported that dislocations glide even at cryogenic temperatures and their motion were impeded by twin boundaries [12,13]. Considering dislocation behavior plays a significant role in the deformation process of materials, a fundamental understanding of the interaction between dislocations and twin boundaries, especially at varying temperatures, is critical to explain the underlying cause of the unusual temperature dependence of the ductility in these alloys.

In this study, we perform molecular dynamics (MD), molecular statics (MS), and nudged elastic band (NEB) simulations to examine the interaction between a dislocation and a twin boundary in Ni-based equiatomic alloys at different temperatures. Particularly, we focus on the screw dislocation (SD)–coherent twin boundary (CTB) interactions since CTBs are observed in FeNiCoCrMn and its subset alloys [12,13], and SDs are expected to have higher stabilities (lower energies) compared to edge dislocations. We perform

* Corresponding author.
E-mail address: xhx@utk.edu (H. Xu).

https://doi.org/10.1016/j.actamat.2021.116886
1359-6454/

simulations for four alloys NiCo, FeNi, FeNiCo, and FeNiCoCr, which have been shown to exist as a single-phase face-centered cubic (fcc) solid solution [10]. The same simulations of pure Ni are also performed for comparison. We find a switch of interaction mechanisms that strongly depends on the temperature, and the SD–CTB interaction contributes to enhanced ductility at low temperatures. This shows the SD–CTB interaction could be at least one of the underlying mechanisms of the unusual temperature dependence of the ductility in these alloys while other factors could also be involved. Further investigations reveal the origin of the temperature dependence in competing mechanisms and shed light on how to control the interaction processes through tuning of fundamental material properties of Ni-based concentrated alloys.

2. Methods

2.1. MD simulations for the SD–CTB interactions

Fig. 1 (a) shows the schematic of the MD simulation cell for investigating the SD–CTB interaction process. The simulation cell consists of two twinned grains, separated by a $\Sigma 3\{111\}\langle 110\rangle$ CTB, and the constituent elements are randomly-distributed in the simulation cell with equal atomic concentration, as shown in Fig. 1 (b). Note, we here focus on pure Ni, FeNi, and FeNiCoCr because we find that interaction processes in NiCo and FeNiCo are similar to those in FeNi and FeNiCoCr in the MS simulations, respectively. The crystal orientation is along X-[1 1 2], Y-[$\bar{1}$ $\bar{1}$ 1], and Z-[$\bar{1}$ 1 0] directions in the original grain, and the cell lengths along the X, Y, and Z directions are $38\sqrt{6}\,a_0$, $54\sqrt{3}\,a_0$, and $8\sqrt{2}\,a_0$, respectively, where a_0 denotes the lattice constant, which is varied in accordance with the temperature. Free boundary conditions are applied along the X and Y directions, while a periodic boundary condition is applied along the Z direction. A screw dislocation with the Burgers vector of $a_0/2[\bar{1}\,1\,0]$ is introduced beside the CTB, following the manner in [18], and the system energy is minimized. This minimization results in the dislocation dissociating into two Shockley partial dislocations with a stacking fault ribbon in-between according to the reaction:

$$a_0/2\left[\bar{1}\,1\,0\right] = a_0/6\left[\bar{2}\,1\,\bar{1}\right] + a_0/6\left[\bar{1}\,2\,1\right] \quad (1)$$

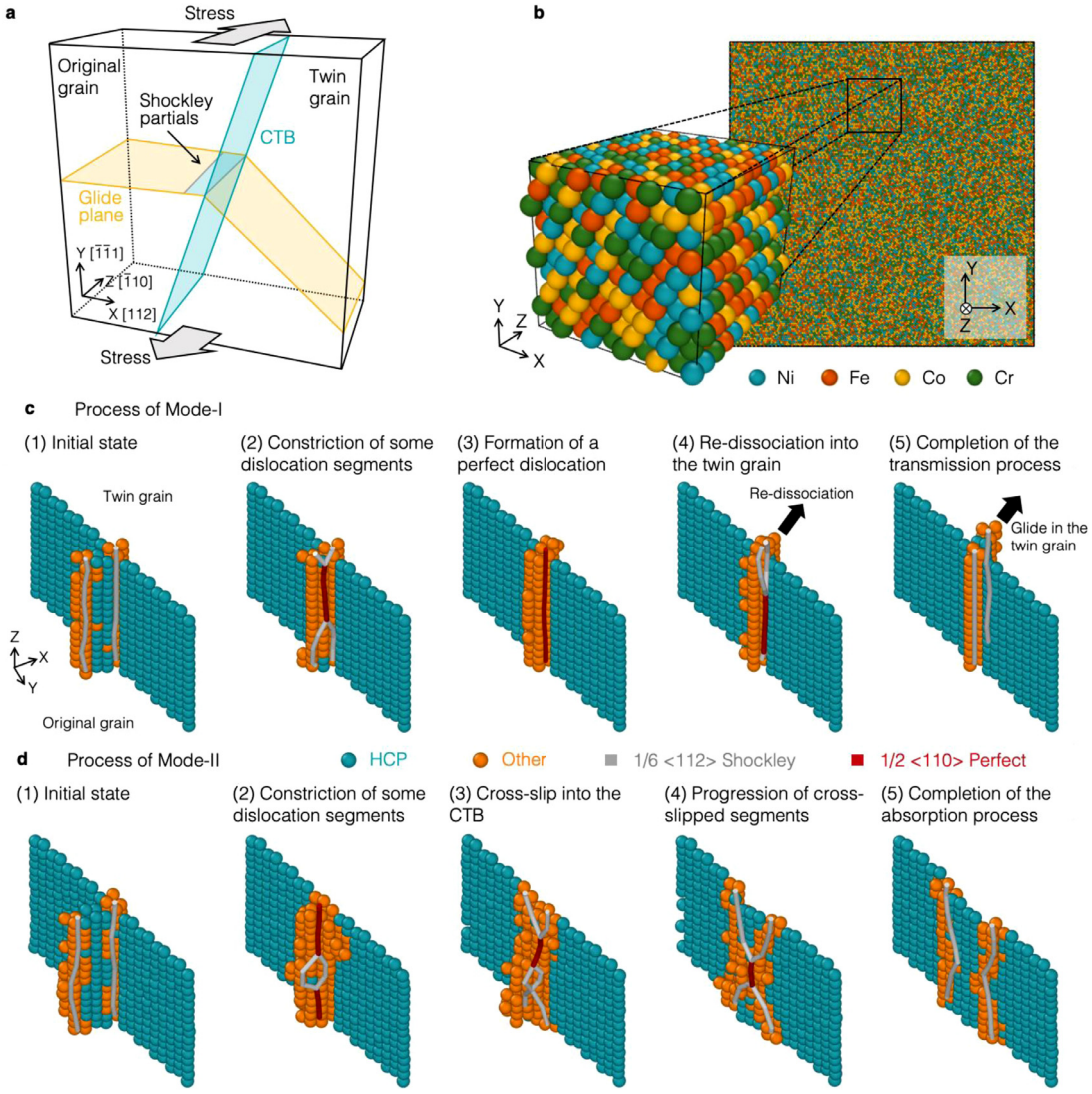

Fig. 1. Simulation set-up and observed interaction mechanisms. (a) Schematic of the simulation setup and the simulation box. (b) A representative atomic configuration of the FeNiCoCr system. (c) Snapshots of the process for Mode-I. (d) Snapshots of the process for Mode-II. Only a representative case for each mode is shown here because the process is essentially the same in all the systems. The processes are visualized by the CNA [21], where blue expresses atoms with the hexagonal closest packed (hcp) structure, namely, stacking fault structure, while orange represents atoms that have neither fcc nor hcp structure. The DXA [22] is also used in analysis, to examine the type of dislocation components. The 1/6 <112> Shockley partial and 1/2 <110> perfect components are displayed with gray and red, respectively. (For interpretation of the references to color in this figure legend, the reader is referred to the web version of this article.)

Then, the system energy minimization is performed again under an applied stress, which is set to 530, 780, and 900 MPa for pure Ni, FeNi, and FeNiCoCr systems, respectively. Note that these stress values need to be chosen carefully because the interaction process could occur even before the system reaches the equilibrium state if the stress is too high while no interaction processes could be observed within the MD timescale if it is too low (further discussion can be found in Supplementary Material). We determine the stress for each system by trial and error, and it is kept constant throughout the simulation. The temperature is set in the range of 100–400 K, where an equilibrium system state is carefully obtained (the details can be found in Supplementary Material). The interatomic interactions in the system are described by an embedded atom method (EAM)-type potential for the HEA FeNiCoCrCu, developed by Farkas et al [19]. At least 15 repeated calculations are performed at each condition while varying the initial distribution of the atomic velocities and distribution of the constituent elements to investigate statistical variations of the results. All the simulations in this study are performed using the large atomic/molecular massively parallel simulator (LAMMPS) [20], and obtained results are visualized using the common neighbor analysis (CNA) [21] and dislocation extraction algorithm (DXA) [22], both of which are implemented in a visualization software, OVITO [23].

2.2. MS simulations for the SD–CTB interactions

We also perform MS simulations of the SD–CTB interactions for pure Ni, NiCo, FeNi, FeNiCo, and FeNiCoCr. The simulation cell geometry and boundary conditions are the same as those in the MD simulations of the SD–CTB interactions, except for the cell length along the *X* direction, which is set to $53\sqrt{6}\ a_0$ (Fig. S1 in Supplementary material). A pair of Shockley partial dislocations is introduced in the same manner as in Subsection 2.1 and is placed ~12 nm from the intersection between the dislocation slip plane and the CTB. Here, we employ constant strain-rate conditions to investigate the SD–CTB interaction process, where a shear strain of 2.0×10^{-5} is incrementally applied by displacing the atoms in the upper and lower *XZ* surfaces. The system energy minimization is performed and the stress of the system is recorded after every strain application. At least 10 repeated calculations are performed for the alloys with different atomic distributions of the constituent elements in order to investigate statistical variations of the results.

2.3. MD simulations for the temperature dependence of $\mu b_p/\gamma_{SFE}$

As discussed later, we find that a non-dimensional parameter, $\mu b_p/\gamma_{SFE}$, is critical for the SD–CTB interactions, consistent with a previous study [24]. Note that μ, b_p, and γ_{SFE} denote the shear modulus, Burgers vector of a partial, and stacking fault energy, respectively, and the $\mu b_p/\gamma_{SFE}$ is related to the equilibrium separation distance of the Shockley partials in the bulk under a no stress condition [25]:

$$\frac{d_{eq}}{b_p} = \frac{(2-3\nu)}{8\pi(1-\nu)}\frac{\mu b_p}{\gamma_{SFE}} \quad (2)$$

where d_{eq} and ν denote the equilibrium separation distance of the partials and Poisson's ratio. We perform MD simulations to investigate the temperature dependence of $\mu b_p/\gamma_{SFE}$ for pure Ni, FeNi, and FeNiCoCr. A pair of Shockley partial dislocations is introduced in the same manner as in Subsection 2.1 at the center of a simulation box with cell lengths of $47\sqrt{6}\ a_0$, $48\sqrt{3}\ a_0$, and $8\sqrt{2}\ a_0$ for *X*-[1 1 2], *Y*-[$\bar{1}$ $\bar{1}$ 1], and *Z*-[$\bar{1}$ 1 0] directions, respectively. Periodic boundary conditions are applied for the *X* and Z directions while a free boundary condition is applied for the *Y* direction. The temperature is set in the range of 100–400 K, depending on the system. The separation distance between the two partials is recorded every 0.1 ps for at least 200 ps after an initial system equilibration of 10 ps at the target temperature. The averaged value is defined as the d_{eq}, which is converted to $\mu b_p/\gamma_{SFE}$, based on Eq. (2). Note that the value of ν is set to 0.3. At least 10 repeated calculations are performed at each condition while varying the initial distribution of the atomic velocities and distribution of the constituent elements to investigate statistical variations of the results.

2.4. NEB simulations for the $\mu b_p/\gamma_{SFE}$ dependence of E_{b1} and E_{b2}

As discussed later, we observe two types of interaction modes in the MD simulations for the SD–CTB interactions, referred to as Mode-I and Mode-II (see Fig. 1 (c) and (d)). We evaluate the $\mu b_p/\gamma_{SFE}$ dependence of the energy barrier of Mode-I (E_{b1}) and Mode-II (E_{b2}) using the climbing NEB simulations [26] to obtain a fundamental understanding of how the $\mu b_p/\gamma_{SFE}$ influences these interaction modes. To isolate the effect of the $\mu b_p/\gamma_{SFE}$ on E_{b1} and E_{b2}, we use four sets of model fcc EAM-type potentials developed by Borovikov et al. [27], which have different γ_{SFE} from each other (from 14.6 to 61.6 mJ m^{-2}) while keeping other significant materials parameters the same, and evaluate the values of E_{b1} and E_{b2} for each potential. Here, while we employ the same simulation cell geometry, manner of dislocation introduction, and boundary conditions as those described in Subsection 2.1, we consider a cylindrical region along the dislocation line with a radius of 10 nm, atoms outside which are fixed during the NEB simulations to improve the computational efficiency (Fig. S5 in Supplementary Material). The transition path is discretized into 64 images, and the fast inertial relaxation engine (FIRE) method is used to move the atoms during the simulations. Iterations are stopped when the maximum two-norm of the force vector per replica is below 0.02 eV Å^{-1}. The detailed procedures to create the initial and final states for Mode-I and Mode-II can be found in Supplementary material. For deriving the value of $\mu b_p/\gamma_{SFE}$ for each potential by Borovikov et al., we prepare a simulation box by introducing a pair of Shockley partial dislocations in the same manner as in Subsection 2.1 and examine d_{eq} at 0 K after the system energy minimization, which is converted to $\mu b_p/\gamma_{SFE}$ based on Eq. (2), where ν is set to 0.3. The simulation cell geometry and the boundary conditions are the same as those described in Subsection 2.3. The derived values of $\mu b_p/\gamma_{SFE}$ for the four potentials are 48.0, 72.0, 143.9, and 239.9, which cover the range of $\mu b_p/\gamma_{SFE}$ by the Farkas potential observed in this study, as seen in Fig. 3 (b).

3. Results and discussion

In the MD simulations for the SD–CTB interactions, we observe two different interaction mechanisms, namely, Mode-I and Mode-II, in Ni-based equiatomic alloys (FeNi and FeNiCoCr) and pure Ni as a function of temperature. For Mode-I, a dislocation transmits into the twin grain by cutting through the CTB (Fig. 1 (c)). In contrast, a dislocation is absorbed by the CTB involving a cross-slip process in Mode-II (Fig. 1 (d)). Different from previous MS simulations, in which only one type of mode was identified for each system with a specific potential [24,28], we observe a switch of the dominant mode in one system as a function of temperature. It should be highlighted here that these two modes have dramatically different contributions to the ductility. While Mode-I enhances the ductility, since the deformation process can propagate across the CTB, the deformation in Mode-II is accumulated within the grain because the dislocation is absorbed by the CTB.

By examining the details of the interaction processes, we observe that all the dislocation segments simultaneously constrict during Mode-I, as shown in Fig. 1 (c), temporarily forming a perfect dislocation on the CTB. The perfect dislocation then starts to

re-dissociate into the twin grain, and once the re-dissociation process is completed, the partial dislocations glide on another slip plane in the twin grain. Meanwhile, the process of Mode-II is very similar to Friedel–Escaig mechanism of cross-slip in fcc metals [29] (Fig. 1 (d)). After the cross-slip, the two partials easily move away from each other on the twin plane because they are not bounded by stacking fault attraction anymore, unlike a dissociation in the bulk. In addition, we set the output interval of the system configuration during the simulations to as short as 40 fs to carefully examine the interaction process; however, simultaneous constriction of all the segments, as in Mode-I, has not been observed. In previous studies, a dislocation absorption by the CTB through cross-slip was certainly observed, but its process was reported to involve the simultaneous constriction of all the segments [24,28]. This is because a quasi-two-dimensional simulation cell was used, in which the length along the dislocation line is very short. Due to this size limitation, constricted and dissociated segments could not form simultaneously in their studies.

Fig. 2 shows the ratio of the number of cases for Mode-I to the total number of repeated calculations at the same condition. It is clearly seen that Mode-I is frequently observed at lower temperatures, namely, below 150 K, 125 K, and 150 K for pure Ni, FeNi, and FeNiCoCr, respectively. In comparison, Mode-II dominantly occurs at higher temperatures, above 200 K, 175 K, and 250 K for pure Ni, FeNi, and FeNiCoCr, respectively. This indicates the SD–CTB interaction contributes to the increased ductility of these alloys at low temperatures, since Mode-I accommodates dislocation motion and therefore leads to more plastic deformation, as mentioned previously. Furthermore, a previous experimental study reported a significantly higher elongation to fracture of these alloys at 77 K than that at 293 K: ~39%, ~47%, and ~50% at 77 K in comparison with ~28%, ~37%, and ~40% at 293 K for pure Ni, FeNi, and FeNiCoCr, respectively [10]. This temperature range is in good agreement with the range for the mode switch observed here, strongly suggesting that the switch of dominant interaction mode for the SD–CTB interaction could be one of the underlying mechanisms that contribute to enhanced ductility at cryogenic temperatures in these alloys.

Fig. 2 also shows the value of E_{b1} and E_{b2} as a function of temperature, estimated from the elapsed time for the interaction to occur in the MD simulations based on the Arrhenius relationship:

$$E_{bi} = \mathrm{kTln}\frac{\Gamma_0}{\Gamma} \quad (i = 1, 2) \tag{3}$$

where k, T, Γ, and Γ_0 stands for the Boltzmann constant, temperature, frequency of the mode, i.e., the reciprocal of the elapsed time, and prefactor, assumed to be 1.0×10^{12} s^{-1}, respectively. The fitted curves of the E_{b1} and E_{b2} based on the analytical model are also drawn in the figures (the detailed derivation of the model is presented below). It is important to note, while both the E_{b1} and E_{b2} decrease as the temperature decreases, E_{b1} exhibits a stronger temperature dependence than the E_{b2}, resulting in a crossover of their trend at a specific temperature.

Fig. 3 (a) shows the reaction strain and stress for the interaction to occur in the MS simulations. Note that only Mode-I is observed in all the MS simulations. This is consistent with the MD results above, where Mode-I occurs dominantly at lower temperatures, and also agrees with previous quasi-static simulations, in which only one type of mode was identified for one system with specific potentials [24,28]. As shown in Fig. 3 (a), it is found that both the reaction strain and stress have a linear dependence on $\mu b_p/\gamma_{SFE}$. The linear relationship between the reaction stress and $\mu b_p/\gamma_{SFE}$ was also reported in a previous study [24]. Furthermore, the MD simulations for the temperature dependence of $\mu b_p/\gamma_{SFE}$ revealed that the $\mu b_p/\gamma_{SFE}$ increases linearly with an increase in the temperature for pure Ni, FeNi, and FeNiCoCr, as shown in Fig. 3 (b). These results suggest that the temperature dependence of the $\mu b_p/\gamma_{SFE}$ could trigger the switch of SD–CTB interaction modes, as observed in Fig. 2.

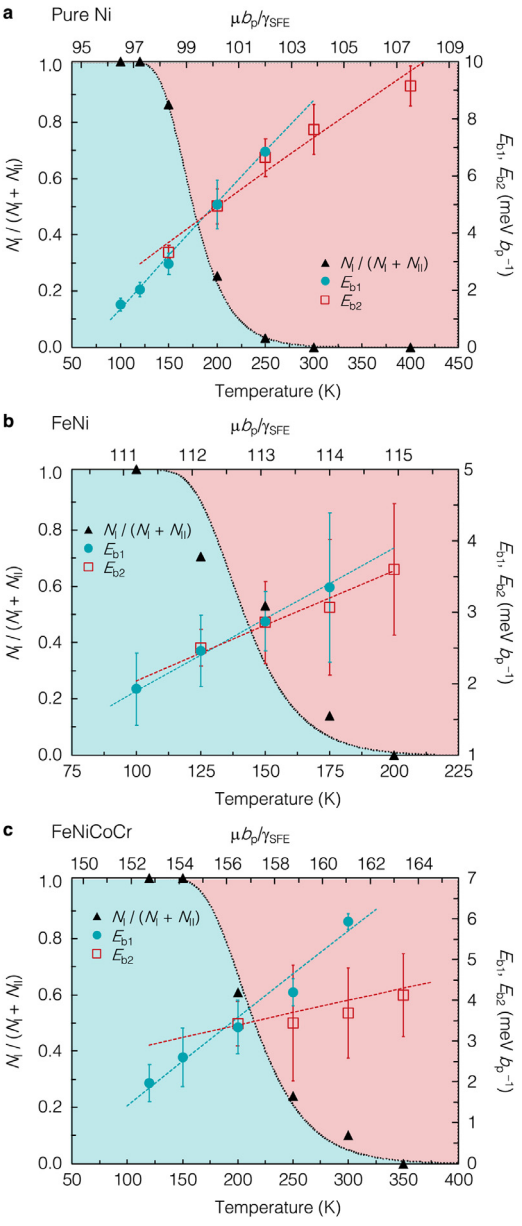

Fig. 2. Temperature dependence of N_I / (N_I + N_{II}), E_{b1}, and E_{b2}. The N_I and N_{II} denote the number of cases for Mode-I and Mode-II, respectively. The value of $\mu b_p/\gamma_{SFE}$ at each temperature is also shown in the upper horizontal axis, which is evaluated from Fig. 3 (b). Error bars denote the standard deviation of the mean. The error bar for E_{b1} at 250 K in pure Ni is not shown because Mode I is observed only in one case under this condition even after more than 30 repeated calculations are performed (further discussion can be found in Supplementary Material).

Fig. 4 (a) and (b) show the $\mu b_p/\gamma_{SFE}$ dependence of E_{b1} and E_{b2} under different stress conditions, evaluated by the NEB simulations with the four interatomic potentials that have different γ_{SFE} from each other [27]. As shown in the figures, E_{b1} exhibits a stronger $\mu b_p/\gamma_{SFE}$ dependence than the E_{b2}, which is consistent with the MD results of the SD–CTB interaction (Fig. 2), obtained using the interatomic potential for the HEA of FeNiCoCrCu [19]. In addition, it is found that both E_{b1} and E_{b2} have a logarithmic dependence on the $\mu b_p/\gamma_{SFE}$, regardless of the stress. The reason for the logarithmic dependence of the E_{b1} is explained using the following discussion based on the elasticity theory. As shown in Fig. 4 (d),

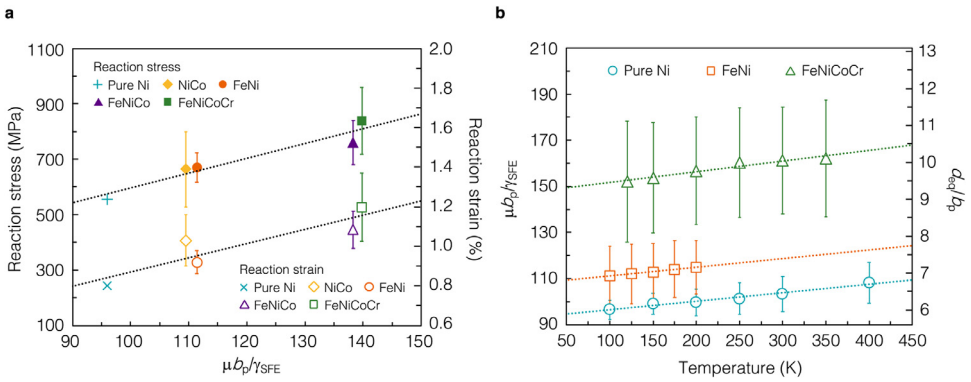

Fig. 3. (a) Reaction stresses and strains for pure Ni, NiCo, FeNi, FeNiCo, and FeNiCoCr, recorded at the moment of the occurrence of Mode-I, which is the only mode observed during the MS simulations. (b) Temperature dependence of $\mu b_p/\gamma_{SFE}$ for Pure Ni, FeNi, and FeNiCoCr, which is evaluated from the d_{eq} using Eq. (2).

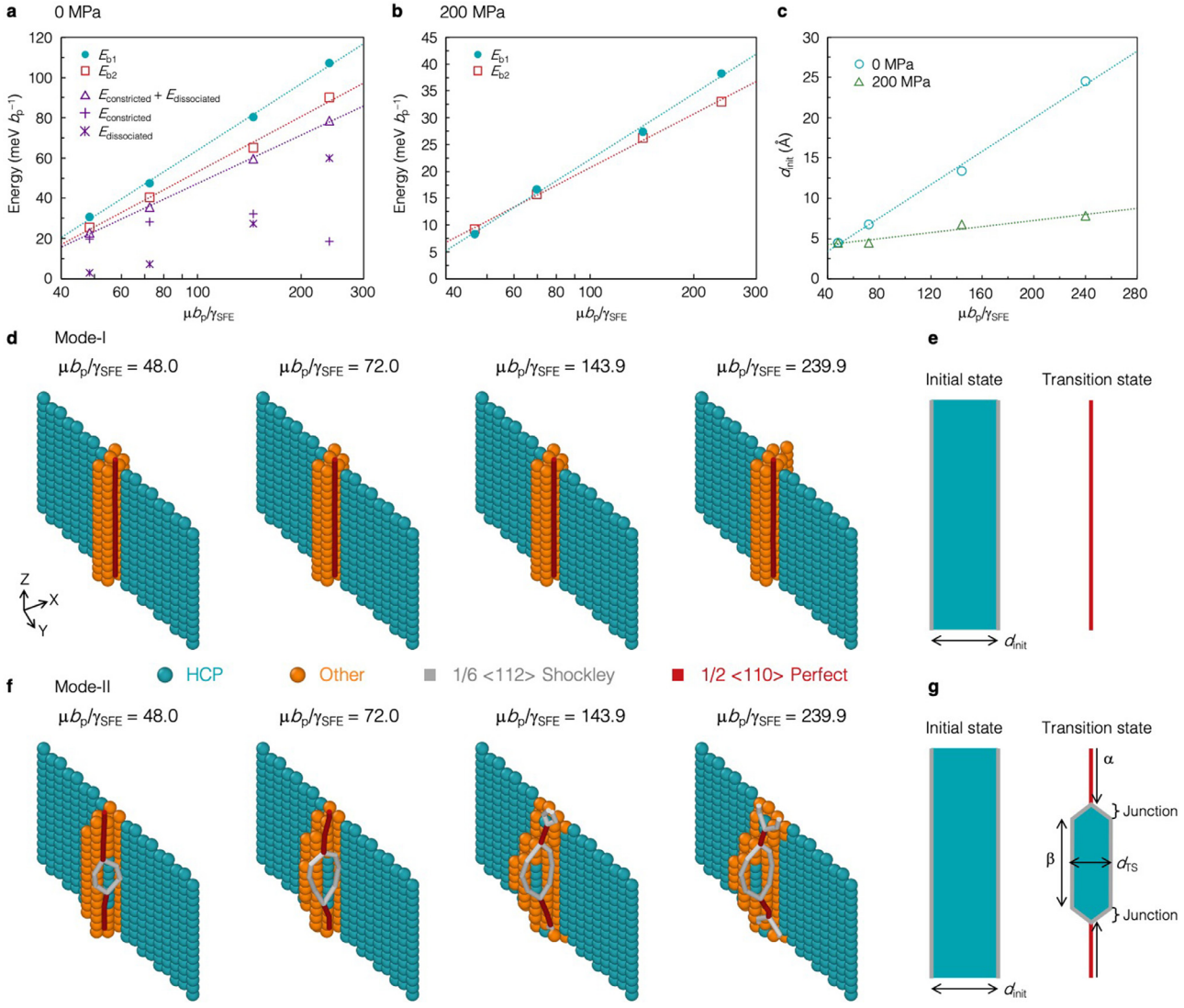

Fig. 4. Evaluation of the $\mu b_p/\gamma_{SFE}$ dependence of the E_{b1} and E_{b2} using the four fcc model potentials, developed by Borovikov et al [27]. (a) Values of E_{b1}, E_{b2}, $E_{constricted}$, and $E_{dissociated}$ as a function of the $\mu b_p/\gamma_{SFE}$ at 0 MPa. (b) Values of E_{b1} and E_{b2} as a function of $\mu b_p/\gamma_{SFE}$ at 200 MPa. (c) Dependence of d_{init} on $\mu b_p/\gamma_{SFE}$. (d) TS configuration of Mode-I at different values of $\mu b_p/\gamma_{SFE}$. (e) Schematic of the initial state and TS configurations of Mode-I. (f) TS configuration of Mode-II at different values of $\mu b_p/\gamma_{SFE}$. (g) Schematic of the initial state and TS configurations of Mode-II.

the transition state (TS) configuration of Mode-I is a perfect dislocation, and the E_{b1} is hence expressed as:

$$E_{b1} = E_{perfect} - E^{init}_{partials} \quad (4)$$

where $E_{perfect}$ and $E^{init}_{partials}$ denote the energy of a perfect dislocation and that of two partials with a separation distance of d_{init}, respectively. Note that the $E_{perfect}$ does not depend on the $\mu b_p/\gamma_{SFE}$, because of the TS configuration (Fig. 4 (d)). The $E^{init}_{partials}$, instead, is influenced by the $\mu b_p/\gamma_{SFE}$ due to (i) the interaction energy between the two partials and (ii) a stacking fault between the partials (Fig. 4 (e)). Therefore, the $E^{init}_{partials}$ dependence on the $\mu b_p/\gamma_{SFE}$ can be modeled by the following equation [25]:

$$E^{init}_{partials} \propto -\frac{\mu b_p^2(2-3\nu)}{8\pi(1-\nu)}\ln\frac{d_{init}}{r_0} + d_{init}\gamma_{SFE} \quad (5)$$

where r_0 denotes the dislocation core radius. As shown in Fig. 4 (c), d_{init} has a linear relationship with the $\mu b_p/\gamma_{SFE}$. This means (i) the first term in Eq. (5) exhibits a logarithmic dependence on $\mu b_p/\gamma_{SFE}$ and (ii) the second term in Eq. (5) has little $\mu b_p/\gamma_{SFE}$ dependence because the effects of the γ_{SFE} is canceled out as a whole. The result is a logarithmic dependence of the $E^{init}_{partials}$ on the $\mu b_p/\gamma_{SFE}$. As a consequence, E_{b1} can be analytically modeled by a logarithmic function of $\mu b_p/\gamma_{SFE}$.

The case for E_{b2} is more complicated because the dislocation configuration at the TS contains both constricted and dissociated components, as shown in Fig. 4 (f). Here, we develop a simple analytical model to understand E_{b2} dependence on the $\mu b_p/\gamma_{SFE}$. As shown in Fig. 4 (g), the TS configuration of Mode-II can be divided into three parts: constricted, dissociated, and junction components. We assume the junction components are similar at different values of $\mu b_p/\gamma_{SFE}$, and their contribution to the $\mu b_p/\gamma_{SFE}$ dependence can therefore be ignored. The E_{b2} can then be expressed as:

$$E_{b2} \propto E_{constricted} + E_{dissociated}$$
$$= \alpha\left(E_{perfect} - E^{init}_{partials}\right) + \beta\left(E^{TS}_{partials} - E^{init}_{partials}\right) \quad (6)$$

where $E_{constricted}$, $E_{dissociated}$, α, β, and $E^{TS}_{partials}$ denote the energy term associated with the constricted component, the energy term associated with the dissociated component, the ratio of the constricted component, the ratio of the dissociated component, and the energy of two partials with a separation distance of d_{TS}, containing a stacking fault in-between, respectively (d_{TS} is the separation distance of the dissociated component at the TS, as shown in Fig. 4 (g)). We evaluate $E_{constricted}$ and $E_{dissociated}$ at different values of $\mu b_p/\gamma_{SFE}$, which are shown as purple symbols in Fig. 4 (a) (the detailed procedure can be found in Supplementary Material). Although $E_{constricted}$ and $E_{dissociated}$ exhibit completely different trends from each other, the sum of them exhibits a clear logarithmic dependence, which is in agreement with the NEB results. Note that the values of the sum from the analytical model are lower than E_{b2} due to the neglect of the junction components. As a consequence, E_{b2} can also be analytically modeled by a logarithmic function of $\mu b_p/\gamma_{SFE}$. Based on the derived logarithmic dependence of E_{b1} and E_{b2}, we draw fitted curves of the E_{b1} and E_{b2} in Fig. 2, which agree very well with MD results. This quantitative agreement further supports: (i) both E_{b1} and E_{b2} have a logarithmic dependence on $\mu b_p/\gamma_{SFE}$; (ii) their magnitudes are different from each other, resulting in a crossover point of E_{b1} and E_{b2} at a specific temperature.

While a specific stress is employed for each simulation in this study, the mode change itself is general for different stress levels but the transition temperature of the two modes could be influenced by the stress, the reasons for which are discussed next. First, a different stress mainly changes the driving force for the glide of the trailing partial toward the leading one, resulting in a change in d_{init} (Fig. 4 (c)), such as d_{init} becoming smaller at higher stresses. Second, if we define ΔE_b as $E_{b1} - E_{b2}$, ΔE_b becomes larger as $\mu b_p/\gamma_{SFE}$ increases, as shown in Fig. 2. Third, d_{init} has a linear relationship with $\mu b_p/\gamma_{SFE}$, as shown in Fig. 4 (c). Combining these, we reach that increasing stresses leads to a smaller ΔE_b (through a smaller d_{init}) and reducing stresses results in a larger ΔE_b (through a larger d_{init}). This means that a different stress level would change the transition temperature of the two modes: a lower stress shifts the transition temperature toward lower while a higher stress shifts it toward higher temperatures. Considering that an experimental study [10] reported the ultimate tensile strength for pure Ni, FeNi, and FeNiCoCr at 77 K is ~550, 830, and 1150 MPa, respectively, the stresses employed in this study are at relatively moderate to high levels. This is necessary so the interaction occurs within the MD timescale, even at very low temperatures. In the experimental timescale, however, much lower stress conditions are enough to induce the SD-CTB interaction, where the transition temperature could be correspondingly changed, depending on the experimental stress conditions.

Since the employed interatomic potential could affect the results of MD simulations in general, we also perform additional MD simulations of the SD–CTB interaction using the 2nd nearest-neighbor modified EAM potential for FeNiCoCrMn HEAs developed by Choi et al. [30] to investigate the influence of the potential on the temperature dependence of the SD–CTB interaction. Here, we focus on only two cases for FeNi, at 77 and 300 K, because the simulations using the Choi potential are computationally expensive. The applied stress is set to 1000 MPa, and five repeated calculations are performed at each temperature. The other conditions are the same as those described in Subsection 2.1. In these simulations, only Mode I occurs at 77 K while Mode II is exclusively observed at 300 K, which is consistent with the results obtained by the Farkas potential, as shown in Fig. 2. This leads to the conclusion that the switch of the dominant interaction mode depending on the temperature is not influenced by the employed potential while the specific temperature of the switch could be different.

4. Conclusions

We conclude the dominant mode of SD–CTB interactions in Ni-based equiatomic alloys strongly depends on the temperature, which could be one of the underlying mechanisms contributing to enhanced ductility at cryogenic temperatures in these alloys, though other factors could also be involved. The detailed investigation of the interaction modes demonstrates the temperature dependence of the dominant interaction mode arises from that of $\mu b_p/\gamma_{SFE}$, which affects E_{b1} and E_{b2} differently. The quantitative agreement between the MD results and developed analytical models strongly support the fidelity of this study. Furthermore, the mechanistic insights and analytical models developed here are essential for a comprehensive understanding of deformation process of fcc HEAs and for the development of strategies to control mechanical properties of advanced structural materials.

Declaration of Competing Interest

The authors declare no competing financial interests.

Acknowledgments

This work is supported by the National Science Foundation under Grant No. DMR-1654438. This work uses the Extreme Science and Engineering Discovery Environment (XSEDE), which is supported by the National Science Foundation grant number TG-DMR170112.

Supplementary materials

Supplementary material associated with this article can be found, in the online version, at doi:10.1016/j.actamat.2021.116886.

References

[1] J.-W. Yeh, S.-K. Chen, S.-J. Lin, J.-Y. Gan, T.-S. Chin, T.-T. Shun, C.-H. Tsau, S.-Y. Chang, Nanostructured high-entropy alloys with multiple principal elements: novel alloy design concepts and outcomes, Adv. Eng. Mater. 6 (2004) 299–303.

[2] B. Gludovatz, A. Hohenwarter, D. Catoor, E.H. Chang, E.P. George, R.O. Ritchie, A fracture-resistant high-entropy alloy for cryogenic applications, Science 345 (2014) 1153–1158.

[3] Z. Zhang, M.M. Mao, J. Wang, B. Gludovatz, Z. Zhang, S.X. Mao, E.P. George, Q. Yu, R.O. Ritchie, Nanoscale origins of the damage tolerance of the high-entropy alloy CrMnFeCoNi, Nat. Commun. 6 (2015) 10143.

[4] B. Cantor, I.T.H. Chang, P. Knight, A.J.B. Vincent, Microstructural development in equiatomic multicomponent alloys, Mater. Sci. Eng. A 375–377 (2004) 213–218.

[5] E.P. George, D. Raabe, R.O. Ritchie, High-entropy alloys, Nat. Rev. Mater. 4 (2019) 515–534.

[6] Z. Li, K.G. Pradeep, Y. Deng, D. Raabe, C.C. Tasan, Metastable high-entropy dual-phase alloys overcome the strength–ductility trade-off, Nature 534 (2016) 227–230.

[7] Y.H. Jo, S. Jung, W.M. Choi, S.S. Sohn, H.S. Kim, B.J. Lee, N.J. Kim, S. Lee, Cryogenic strength improvement by utilizing room-temperature deformation twinning in a partially recrystallized VCrMnFeCoNi high-entropy alloy, Nat. Commun. 8 (2017) 15719.

[8] F. Otto, A. Dlouhy, Ch. Somsen, H. Bei, G. Eggeler, E.P. George, The influences of temperature and microstructure on the tensile properties of a CoCrFeMnNi high-entropy alloy, Acta Mater 61 (2013) 5743–5755.

[9] A. Gali, E.P. George, Tensile properties of high- and medium-entropy alloys, Intermetallics 39 (2013) 74–78.

[10] Z. Wu, H. Bei, G.M. Pharr, E.P. George, Temperature dependence of the mechanical properties of equiatomic solid solution alloys with face-centered cubic crystal structures, Acta Mater 81 (2014) 428–441.

[11] O.R. Ritchie, The conflicts between strength and toughness, Nat. Mater. 10 (2011) 817–822.

[12] Q. Ding, X. Fu, D. Chen, H. Bei, B. Gludovatz, J. Li, Z. Zhang, E.P. George, Q. Yu, T. Zhu, R.O. Ritchie, Real-time nanoscale observation of deformation mechanisms in CrCoNi-based medium- to high-entropy alloys at cryogenic temperatures, Mater. Today 25 (2019) 21–27.

[13] J. Miao, C.E. Slone, T.M. Smith, C. Niu, H. Bei, M. Ghazisaeidi, G.M. Pharr, M.J. Mills, The evolution of the deformation substructure in a Ni-Co-Cr equiatomic solid solution alloy, Acta Mater. 132 (2017) 35–48.

[14] Y. Wang, B. Liu, K. Yan, M. Wang, S. Kabra, Y.-L. Chiu, D. Dye, P.D. Lee, Y. Liu, B. Cai, Probing deformation mechanisms of a FeCoCrNi high-entropy alloy at 293 and 77 K using in situ neutron diffraction, Acta Mater. 154 (2018) 79–89.

[15] Q. Lin, J. Liu, X. An, H. Wang, Y. Zhang, X. Liao, Cryogenic-deformation-induced phase transformation in an FeCoCrNi high-entropy alloy, Mater. Res. Lett. 6 (2018) 236–243.

[16] K.V.S. Thurston, A. Hohenwarter, G. Laplanche, E.P. George, B. Gludovatz, R.O. Ritchie, On the onset of deformation twinning in the CrFeMnCoNi high--entropy alloy using a novel tensile specimen geometry, Intermetallics 110 (2019) 106469.

[17] G. Laplanche, A. Kostka, O.M. Horst, G. Eggeler, E.P. George, Microstructure evolution and critical stress for twinning in the CrMnFeCoNi high-entropy alloy, Acta Mater. 118 (2016) 152–163.

[18] T. Hatano, T. Kaneko, Y. Abe, H. Matsui, Void-induced cross slip of screw dislocations in fcc copper, Phys. Rev. B 77 (2008) 064108.

[19] D. Farkas, A. Caro, Model interatomic potentials and lattice strain in a high-entropy alloy, J. Mater. Res. 33 (2018) 3218–3325.

[20] S. Plimpton, Fast parallel algorithms for short-range molecular dynamics, J. Comput. Phys. 117 (1995) 1–19.

[21] H. Tsuzuki, P.S. Branicio, J.P. Rino, Structural charac- terization of deformed crystals by analysis of common atomic neighborhood, Comput. Phys. Commun. 177 (2007) 518–523.

[22] A. Stukowski, V.V. Bulatov, A. Arsenlis, Automated identification and indexing of dislocations in crystal interfaces, Model. Simul. Mater. Sci. Eng. 20 (2012) 085007-1–085007-16.

[23] A. Stukowski, Visualization and analysis of atomistic simulation data with OVITO – the Open Visualization Tool, Model. Simul. Mater. Sci. Eng. 18 (2010) 015012-1–015012-7.

[24] M. Chassagne, M. Legros, D. Rodney, Atomic-scale simulation of screw dislocation/coherent twin boundary interaction in Al, Au, Cu and Ni, Acta Mater. 59 (2011) 1456–1463.

[25] J.P. Hirth, J. Lothe, Theory of dislocations, McGraw-Hill, New York, 1968.

[26] G. Henkelman, B.P. Uberuaga, H.A. Jonsson, climbing image nudged elastic band method for finding saddle points and minimum energy paths, J. Chem. Phys. 113 (2000) 9901–9904.

[27] V. Borovikov, M.I. Mendelev, A.H. King, R. LeSar, Effect of stacking fault energy on mechanism of plastic deformation in nanotwinned FCC metals, Modelling Simul. Mater. Sci. Eng. 23 (2015) 055003-1–055003-16.

[28] Z.-H. Jin, P. Gumbsch, E. Ma, K. Albe, K. Lu, J. Hahn, H. Gleiter, The interaction mechanism of screw dislocations with coherent twin boundaries in different face-centred cubic metals, Scripta Mater. 54 (2006) 1163–1168.

[29] B. Escaig, Cross slip of screw dislocations in F.C.C. structures, J. Phys. France 29 (1968) 225–239.

[30] W.-M. Choi, Y.H. Jo, S.S. Sohn, S. Lee, B.-J. Lee, Understanding the physical metallurgy of the CoCrFeMnNi high-entropy alloy: an atomistic simulation study, npj Comput. Mater. 4 (2018) 1.